

# RSC Advances



This is an *Accepted Manuscript*, which has been through the Royal Society of Chemistry peer review process and has been accepted for publication.

*Accepted Manuscripts* are published online shortly after acceptance, before technical editing, formatting and proof reading. Using this free service, authors can make their results available to the community, in citable form, before we publish the edited article. This *Accepted Manuscript* will be replaced by the edited, formatted and paginated article as soon as this is available.

You can find more information about *Accepted Manuscripts* in the [Information for Authors](#).

Please note that technical editing may introduce minor changes to the text and/or graphics, which may alter content. The journal's standard [Terms & Conditions](#) and the [Ethical guidelines](#) still apply. In no event shall the Royal Society of Chemistry be held responsible for any errors or omissions in this *Accepted Manuscript* or any consequences arising from the use of any information it contains.

# Creep-resistant behavior of beta-polypropylene with different crystalline morphology

Chenfei Jia<sup>a</sup>, Xia Liao<sup>a\*</sup>, Jingjun Zhu<sup>b</sup>, Zhu An<sup>b</sup>, Qiongwen Zhang<sup>a</sup>, Qi Yang<sup>a</sup>,

Guangxian Li<sup>a\*</sup>

<sup>a</sup> College of Polymer Science and Engineering, State Key Laboratory of Polymer Materials Engineering, Sichuan University, Chengdu, Sichuan 610065, China

<sup>b</sup> Key Laboratory of Radiation Physics and Technology of Ministry of Education, Institute of Nuclear Science and Technology, Sichuan University, Chengdu, Sichuan 610064, China

Corresponding authors:

Xia Liao

Tel.:+86-28-8540 8361; E-mail: xiao@scu.edu.cn

Guangxian Li

Tel.:+86-28-8546 9011; E-mail: guangxianli@scu.edu.cn

## Abstract

The  $\beta$ -phase isotactic polypropylene ( $\beta$ -iPP) specimens with different contents of  $\beta$ -phase nucleating agent were employed to investigate the deformation-induced microstructure evolution during creep behavior. Morphological investigations by SEM showed that the crystalline morphologies of  $\beta$ -iPP were controlled by the content of the  $\beta$ -phase nucleating agent, namely, well-developed  $\beta$ -spherulites induced by low content of  $\beta$ -phase nucleating agent, bundle-like morphology with imperfect spherulites induced by middle content of  $\beta$ -phase nucleating agent and needle-like morphology induced by high content of  $\beta$ -phase nucleating agent. It was interesting to observe that all samples with different contents of  $\beta$ -phase nucleating agent showed similar  $\beta/\alpha$  transformation process. However, well-developed  $\beta$ -spherulites, which have integrated crystalline structure, showed bad creep resistance compared with the crystalline morphology nucleated by higher contents of  $\beta$ -phase nucleating agent. For bundle-like morphology, the crystalline phase was imperfect and obtained larger long spacing, resulting in better creep resistance. With respect to needle-like morphology, the crystalline phase was disordered and owned largest long spacing, resulting in best creep resistance. The results of this work revealed that the creep resistance would be different with different crystalline morphologies. On the other hand, this work provided the evolution of microstructure during deformation to further explain the molecular mechanism of fatigue failure for creep.

**Keywords:** creep resistance,  $\beta$ -iPP, microscope deformation

## Introduction

Isotactic polypropylene (iPP) has been widely used as a kind of commodity plastics with combination of good mechanical properties and low cost. For the recent years, to even further expand the possible application of this material, it is interesting to toughen iPP by either adding modifiers like rubbers [1] or modifying the crystal structure of the polymer [2]. Isotactic polypropylene is a classic polymorphic material having four crystal modifications including monoclinic alpha phase, trigonal beta phase, orthorhombic gamma phase, and smectic mesophase [3-5]. Alpha phase is thermodynamically the most stable crystalline phase of iPP, which can be obtained under normal processing conditions [6]. Beta phase is thermodynamically less stable than alpha phase, and difficult to be achieved under normal processing conditions, but can be induced by shear [7-11], temperature gradient [12,13] or adding special beta-nucleating agents [14-17]. The unstable gamma modification and smectic mesophase are rarely seen in industrial manufacture [18]. The different behaviors of iPP with beta phase on static and short-time dynamic mechanical have been investigated by other groups [19,20]. However, to the best of our knowledge, less investigation has been done to study the change of beta modification in creep behavior.

Recently, increasing attentions have been paid to shear experiments under constant stress, i.e. creep deformation [21-24]. Creep is a time-dependent deformation, which takes place under stress lower than the yielding strength of materials. According to the previous studies, there are four stages on the entire process of creep deformation,

namely (i) instantaneous deformation, (ii) primary creep, (iii) secondary creep, (iv) tertiary creep [25]. The instantaneous elongation owing to the elastic or plastic deformation of polymer soon after the external load applied is almost independence of time. On the primary creep stage, the creep rate begins with a relatively high value, and then decreases rapidly with time. In this region, the strain may be resulted from the slippage of crystal and the orientation of polymer chains under persistent stress. After a period of time, the creep behavior reaches a steady-stage value on the secondary creep stage with viscoelastic flow in the polymer, which has the longest duration on the creep behavior. Finally, the sample goes into the tertiary creep stage, where the creep rate increases rapidly occurring final creep rupture or advanced necking. Drozdov et al. [26-28] successfully got some adjustable parameters fitting the experimental data with derived constitutive equations to predict creep-failure of polypropylene. Ediger et al. [29] showed the changes in segmental mobility during tensile creep deformation of polymer glasses and discovered that no simple mechanical variable was likely to exhibit a simple relationship with molecular mobility universally. Vas et al. [30] predicted the creep strain of fatigue failure depending on the creep load using Weibull distribution based approximations for the measured curves and found that the parameters meet with the measurements.

Although considerable researchers have paid attentions to the macroscopically engineering mechanic of polymer materials during creep deformation, rather less research has been paid to the root reasons caused by microstructure changes. While the microstructure changes during the creep are little investigated, the deformation of

polymer under uniaxial tensile has been well documented, such as the deformation of spherulites under cold drawing [31,32], intralamellar slipping of crystalline blocks and stress-induced crystalline block disaggregation-recrystallization process at critical strain [33,34], free volume changes during deformation at room temperature [35,36]. Brown et al. [37,38] have shown measurements on the development of crystalline lattice during deformation of polytetrafluoroethylene (PTFE) utilizing neutron diffraction measurements. The results revealed that the vast majority of deformation in PTFE was taken up by the amorphous phase. Based on the similarity between uniaxial tensile and creep, it is reasonable to draw lessons from uniaxial tensile to the research of the creep behavior.

Our previous research carried out the hierarchical microstructure changes and molecular deformation mechanism of pure polypropylene during creep [39]. However, the reasons and mechanisms of fatigue failure involved on the creep process have not been completely understood yet. Since the mechanical properties of polymer depend on its microstructure and morphology, it is essential to probe into the creep behavior of the material with different hierarchical microstructures, to gain further insight into the molecular deformation mechanisms and to provide possible routes for properties improvement and service lifetime prediction of the material. For these purposes, our main objective is to investigate the creep performance of  $\beta$ -iPP with different crystalline morphologies which are obtained by various contents of beta-nucleating agent. The experiments were processed under certain stress (375 N) and temperature (100 °C). The influence of different contents of  $\beta$ -phase nucleating agent on the creep

behavior of beta-iPP was investigated. The microstructure change and crystal transition were synchronously investigated. Furthermore, the relationship between crystal and amorphous during deformation was discussed.

## Experimental

### Materials

The PP used in this study was supplied by Lanzhou Petrochemical Company, China. The molecular weights were  $M_w = 3.27 \times 10^5$  g/mol and  $M_n = 8.72 \times 10^4$  g/mol. For the  $\beta$ -phase nucleating agent of iPP, an aryl amide derivative (trade name TMB-5) was provided by Shanxi Provincial Institute of Chemical Industry, China.

### Sample Preparation

To achieve good dispersion of the nucleating agent in iPP, a two-step process was employed to prepare the materials. A master batch containing 5 wt%  $\beta$ -phase nucleating agent in iPP was first prepared by melting blending of TMB-5 and iPP, and then the master batch was melt blended with iPP to obtain a  $\beta$ -phase nucleating agent concentration of 0.05, 0.2, 0.3 and 0.6 wt%. For convenience, samples with TMB-5 are coded with its concentration. IPP/0.05TMB stands for iPP nucleated with 0.05% TMB-5. The mixing process of the materials was conducted in an internal mixer (XSS-300) at 60 rpm and 190 °C for 6 min.

Then dumbbell-shaped samples with a total length of 120 mm and gauge dimensions  $45 \times 20 \times 2.5$  mm<sup>3</sup> were compression molded at 200 °C and 10 MPa for 5

min. Subsequently, the samples were slowly cooled down to room temperature under the nature state. Before drawing, they were dried for 24 h at 60 °C to erase the residual stress and local orientation.

### **Creep Test**

Each sample was prepared to different final strains at 100 °C with constant force  $F = 375$  N, using a multifunction stress aging testing machine. Once reaching the strain needed, the samples were rapidly quenched by a liquid nitrogen gun, and metal frames were applied to preserve the deformation by fixing the samples. Due to difference of measuring method, the deformation could be preserved during XRD/SAXS measurements, whereas the elastic part of the deformation has to relax in the case of DSC/SEM measurements. The neck part of creep samples after being stretched to specify strains were chosen for subsequent tests. It should be pointed out that, the actual cross-section area is changed with time on the process of tensile creep deformation. In this work, only engineering stress was determined without considering the decrease of cross-section area of samples during creep deformation.

### **Scanning Electron Microscope (SEM)**

The morphology of the crystalline regions in PP samples was studied via SEM. At room temperature, the samples were etched for 12 h with an etchant containing 1.3 wt.% potassium permanganate ( $\text{KMnO}_4$ ), 32.9 wt.% concentrated sulfuric acid ( $\text{H}_2\text{SO}_4$ ), and 65.8 wt.% concentrated phosphoric acid ( $\text{H}_3\text{PO}_4$ ). After that, the

samples were successively soaked for 5h at room temperature in the dilute sulphuric acid and deionized water to remove the impurity. After covered with a thin layer of gold, the etched surface was observed by an SEM instrument (model JSM-5900LV) operating at 20 kV.

### **Small-angle X-ray scattering (SAXS)**

SAXS experiments were carried out on a modified Xeuss system of Xenocs France equipped with a semiconductor detector (Pilatus 100 K, DECTRIS, Swiss) attached to a multilayer focused Cu K $\alpha$  X-ray source (GeniX3D Cu ULD, Xenocs SA, France), generated at 50 kV and 0.6 mA. The wavelength of the X-ray radiation was 0.154 nm. The sample-to-detector distance was 2502 mm, and the effective range of the scattering vector  $q$  ( $q = 4\pi(\sin\theta)/\lambda$ , where  $2\theta$  is the scattering angle and  $\lambda$  is the wavelength) was 0.071–0.796 nm $^{-1}$ . Each SAXS pattern obtained in the center of the sample was collected within 30 min which was then background corrected and normalized using the standard procedure. One dimensional scattering intensity distributions have been obtained by integrating the two-dimensional scattering patterns. The experiments were carried out in Changchun Institute of Applied Chemistry, Chinese Academy of Sciences. From the intensity distributions, the long spacing values ( $d_{ac}$ ) for the sample are calculated using the Bragg equation:

$$d_{ac} = \frac{2\pi}{q} \quad (1)$$

For systems with a structure of stacks of lamellae, the correlation function [40] shows

characteristic features that should allow the long spacing defined as the average thickness of a lamella together with one interlamellar amorphous layer measured along the lamellar.

### Differential Scanning Calorimetry (DSC)

Measurements were carried out on a TA Instruments DSC-Q20 fitted with a nitrogen purge chamber, applying heating and cooling rates of 10 K/min in a temperature range between 40 and 200 °C. For clarity, the measured during the heat were shown in a restricted temperature range. During the heating process, the melting behavior can reflect the crystalline structure formed during the compression-molding processing or influenced during the creep measurement, which is very important in analyzing the possible  $\beta$ - $\alpha$  transformation mechanism. The value of crystallinity ( $X_c$ ) for each phase was calculated by

$$X_c = \frac{\Delta H_m}{\rho \times \Delta H_m^0} \quad (2)$$

where  $\rho$  is the weight fraction of iPP in corresponding sample,  $\Delta H_m$  is the DSC measured value of fusion enthalpy, and  $\Delta H_m^0$  is the fusion enthalpy of completely crystalline iPP. Here, the values of  $\Delta H_m^0$  for  $\alpha$ -iPP and  $\beta$ -iPP are selected as 177.0 and 168.5 J/g [41], respectively. Because the DSC curves of some samples exhibit both  $\alpha$ - and  $\beta$ -crystal, the fusions were determined according to an approximate method [42]. Due to partial  $\beta$ -iPP will transform into  $\alpha$ -iPP during DSC scan, leading to the increase of  $X_{c\alpha}$ , the fraction of  $\beta$ -iPP obtained by DSC measurement will be lower than the value measured by XRD. However, the variation trends of both  $\alpha$ -iPP

and  $\beta$ -iPP can be achieved and the data are acceptable to some extent.

### X-ray diffraction (XRD)

XRD analysis was performed with a Philips X Pert PRO diffractometer (Holland) using an accelerating voltage of 40 KV. All curves were recorded in the plane perpendicular to the sample surface, parallel to the drawing direction, in the scan interval  $2\theta = 5^\circ$ – $40^\circ$  using  $\text{CuK}_\alpha$  radiation ( $\lambda = 0.154$  nm). The interlayer spacing ( $d_{001}$ ) was calculated using the Bragg equation  $\lambda = 2d\sin\theta$ , where  $\lambda$  is the wavelength. The relative crystallinity of  $\beta$ -phase ( $K_{\beta\text{-XRD}}$ ) was calculated from XRD diffractograms according to the following methodology developed by Turner Jones [43]:

$$K_{\beta\text{-XRD}} = \frac{H_{300}^\beta}{H_{110}^\alpha + H_{040}^\alpha + H_{130}^\alpha + H_{300}^\beta} \quad (3)$$

where height  $H_{110}^\alpha$ ,  $H_{040}^\alpha$  and  $H_{130}^\alpha$  are the intensities of the (110), (040) and (130) reflections of the  $\alpha$ -iPP, respectively, and  $H_{300}^\beta$  is the intensity of (300) reflection of  $\beta$ -iPP. This parameter  $K_{\beta\text{-XRD}}$  is only a relative measure of the amount of  $\beta$ -phase in the samples. It couldn't represent the absolute quantity of  $\beta$ -phase in the samples. It provides the information about the variation trend of the  $\beta$ -phase fraction when the samples are prepared in the same way and the measurement condition is completely the same. The strain dependence of the full width at half maximum (FWHM) of the diffraction profile is evaluated for the (110) reflection. The increase of the FWHM means that the crystallites become smaller in size and/or disordered remarkably during the deformation.

## Positron annihilation lifetime spectroscopy (PALS)

The positron annihilation lifetime spectroscopy was measured using a fast-slow coincidence system equipped with BaF<sub>2</sub> crystals. The full width of half-maximum (FWHM) of the time resolution function was 226 ps and the channel width was 12.37 ps. Two identical samples were sandwiched around a  $2 \times 10^5$  Bq <sup>22</sup>Na positron source that was encapsulated between two 7 μm sheets of aluminum foils. The spectroscopy contained  $2.5 \times 10^6$  coincidence counts sufficiently high to be analyzed with LT9.0 software and was decomposed into four discrete lifetime components. The variance of fit was between 0.9 and 1.0 for all performed analyzes. Accompanied with each o-Ps lifetime, a relative intensity was obtained from the PALS measurements, which expressed the relative probability of o-Ps formation.

## Results and discussion

### Creep behavior of β-iPP

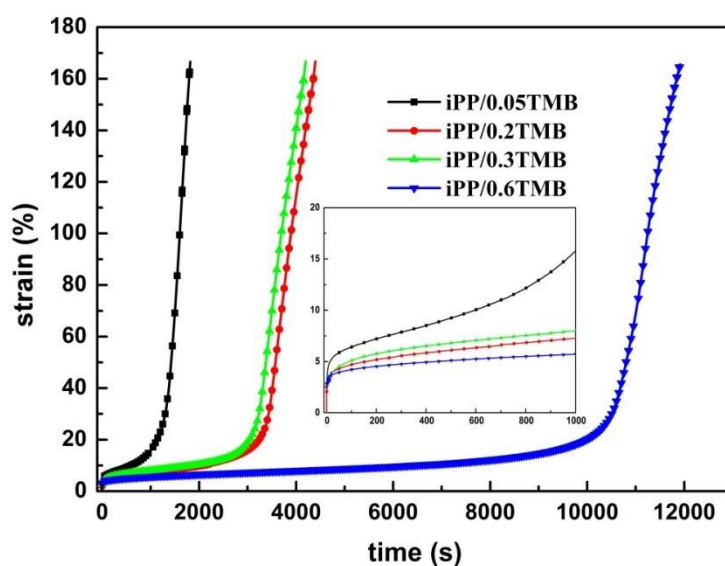


Figure 1 Creep curves of beta-iPP with different contents of  $\beta$ -phase nucleating agent under constant force  $F = 375$  N at  $100$  °C. The inset plot shows enlarged image of instantaneous and primary stages

Figure 1 shows common creep curves of iPP/0.05TMB, iPP/0.2TMB, iPP/0.3TMB and iPP/0.6TMB. The force was preserved constant at 375 N. From these curves, increase strains are monitored as a function of time. On the instantaneous deformation stage, strain of iPP/0.05TMB grows sharply within seconds to reaches about 5%. On the following primary creep stage, the strain rate of iPP/0.05TMB reduces with time to get into a steady stage, the secondary creep region. On this stage, the strain rate is nearly constant. And it occupied most time of the whole creep behavior. At the end of this stage, for iPP/0.05TMB, the strain rate begins to increase after the strain of 11%, which is the start of the tertiary creep region and defined as the fatigue failure point. Then the strain rate increases sharply until deformation quanta is 57%, namely completely fatigue failure point. After this point, the strain rate would slightly decrease. Finally, the curve of iPP/0.05TMB sample becomes sharp with a high strain rate. It should be noticed that, other contents of  $\beta$ -iPP show the similar shape of creep curves. On the instantaneous deformation stage of creep measurement, they suffer the elastic deformation process until the strain increases up to the primary creep stage, which is independent of time. On the following primary creep stage, the creep rate starts at a relatively high value, while decreases rapidly with time, which may be resulted from the slippage and orientation of polymer chains under persistent stress. Then the creep rate reaches a steady-state value on the secondary creep stage, in which the duration is relatively long and the viscoelastic flow occurs. Finally, the

samples fall into the tertiary creep stage, where the creep rate would keep in high level until final creep rupture, as illustrated in Figure 1.

It is important to investigate the crystalline morphologies to better understand the evolution mechanism of the macroscopic creep behavior for  $\beta$ -iPP. Figure 2 shows the supermolecular structures of beta-iPP with different contents of  $\beta$ -phase nucleating agent before deformation. The pictures come through combining of chemical etching and SEM. Agreeing well with the observations reported in the literatures [44-46], the content of 0.05 wt% is the critical  $\beta$ -phase nucleating agent content for iPP and the higher contents of 0.2, 0.3 and 0.6 wt% are the supercritical. For the crystalline morphology shown in Figure 2, iPP/0.05TMB reveals the well-developed  $\beta$ -spherulites whereas iPP/0.2TMB and iPP/0.3TMB reveals the bundle-like morphology instead of distinctly developed spherulites. Furthermore, it is observed that the TMB-5 aggregates into needle-like nucleation structure at highest concentration of 0.6 wt%.

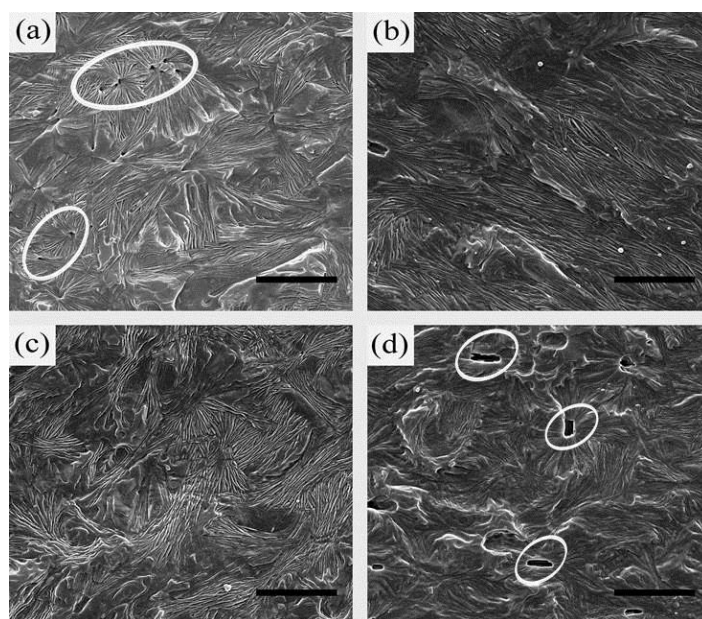


Figure 2 SEM images showing the typical supermolecular structures of (a)

iPP/0.05TMB, (b) iPP/0.2TMB, (c) iPP/0.3TMB and (d) iPP/0.6TMB. Scale bars denote  $3\mu\text{m}$ .

As listed in table 1, both DSC and XRD measurements reveal that the four specimens owning different contents of  $\beta$ -phase nucleating agent and crystalline morphologies exhibit close content of  $\beta$ -phase. However, there is a great difference among the curves in the time scale. In Figure 1, iPP/0.05TMB goes through the shortest time to reach the fatigue failure point whereas iPP/0.2TMB and iPP/0.3TMB experience similar and longer time. And then, iPP/0.6TMB spends the longest time to be fatigue failure. The difference creep resistance is mainly due to the various crystalline morphologies, which are created by different contents of  $\beta$ -phase nucleating agent, as shown in Figure 2. Besides that, in Table 1, iPP/0.2TMB and iPP/0.3TMB show similar long spacing, which are longer than iPP/0.05TMB and shorter than iPP/0.6TMB. The different long spacing listed in Table 1 which was calculated from different curves of 1D scattering intensity distributions of various contents of  $\beta$ -iPP shown in Figure 3 should be another factor for the different creep resistance.

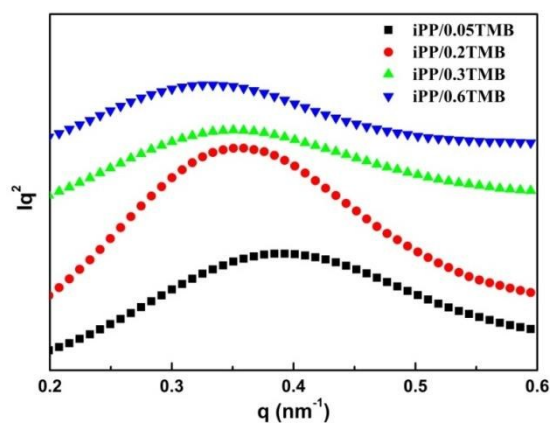


Figure 3 1D scattering intensity distributions at different contents of  $\beta$ -phase

nucleating agent as indicated on the graph.

Table 1 Various properties of undeformed samples with different nucleating contents.

$\epsilon_c$ : strain of critical fatigue failure point;  $K_\beta$ : relative crystallinity of beta-phase measured by XRD;  $d_{ac}$ : long spacing measured by SAXS;  $X_{c\beta}$ : crystallinity of beta-phase measured by DSC.

<b><math>\beta</math>-phase nucleating agent</b>	<b>0.05</b>	<b>0.2</b>	<b>0.3</b>	<b>0.6</b>
$\epsilon_c$ (%)	11	11	11	11
$K_\beta$ (%)	87.1	86.4	85.6	87.5
$d_{ac}$ (nm)	16	17	17	19
$X_{c\beta}$ (%)	22.7	25	23.4	24.6

### Crystalline structure evolution during creep deformation

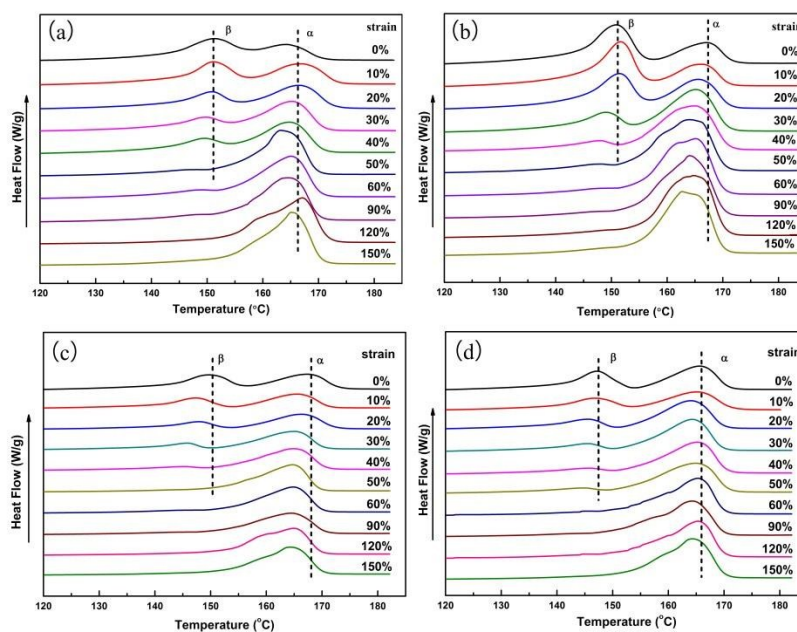


Figure 4 DSC melting curves of (a) iPP/0.05TMB, (b) iPP/0.2TMB, (c) iPP/0.3TMB

and (d) iPP/0.6TMB samples obtained at different strains as indicated on the graphs.

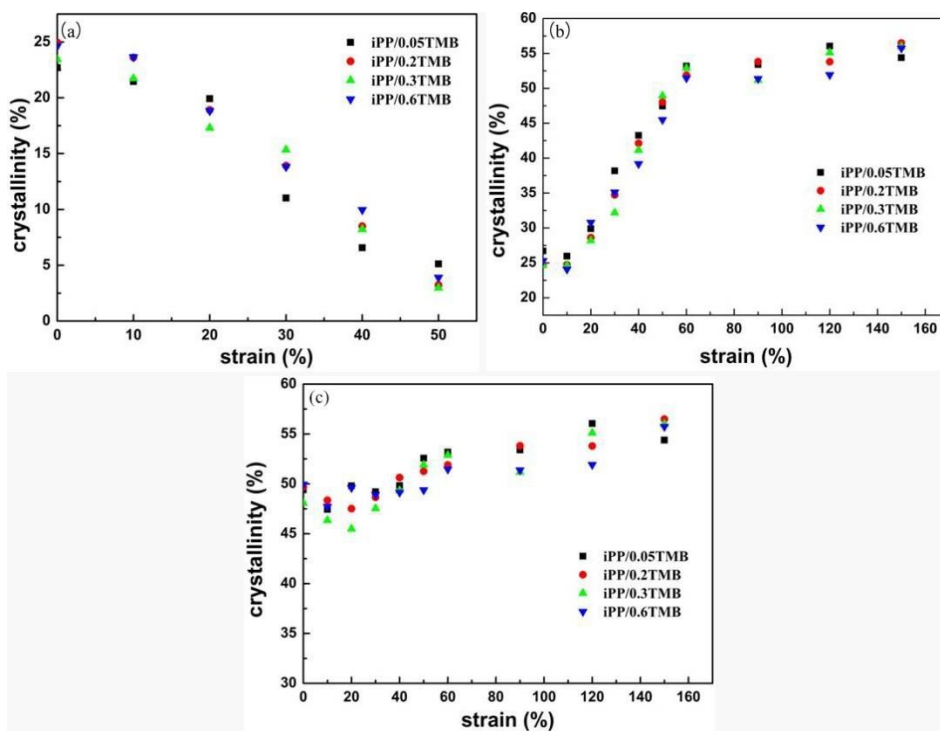


Figure 5 The variation of crystallinity of (a)  $\beta$ -phase, (b)  $\alpha$ -phase and (c)  $\beta + \alpha$  for samples of different nucleating contents with different strains.

The melting behaviors of beta-iPP specimens obtained at different strains are exhibited in Figure 4. For iPP/0.05TMB, two main fusion peaks of undeformed samples are observed at around 151.5 °C and 164 °C, indicating the fusion of  $\beta$ -iPP and  $\alpha$ -iPP, respectively [47]. Before being stretched at complete fatigue failure point (strain  $\approx$  60%), the fusion peak of  $\alpha$ -iPP seems stronger and stronger with the increasing strain, whereas the fusion peak of  $\beta$ -iPP which reflects the content of  $\beta$ -iPP reduces to nearly disappear. This is also shown by the variation of crystallinity for  $\beta$ -phase ( $X_{c\beta}$ ) with strain in Figure 5. The  $X_{c\beta}$  gradually decreases from 22% to 5%. Meanwhile, the melt temperature of  $\beta$ -phase ( $T_{m\beta}$ ) turns into lower and lower temperature gradually. With the further increase of the strain ( $\geq$  60%), the fusion peak

of  $\beta$ -iPP becomes very weak, whereas the fusion of  $\alpha$ -iPP predominates on the following heating process. It is believed that the smaller and smaller fusion peak of  $\beta$ -phase during creep deformation exhibiting the behavior of  $\beta/\alpha$  transformation in this experiment. Besides that, it is interesting to notice the change of  $T_{m\beta}$  after being stretched. It maintains invariable in instantaneous deformation and primary creep region (strain  $\leq 10\%$ ) and decreases gradually after the strain of fatigue failure ( $> 10\%$ ). This means that, at low strain, instead of changing the lamellae structure of  $\beta$ -iPP, the applied stress mainly promotes the orientation and deformation of amorphous, which agrees with the result got from Brown et al. [37,38]. However, at middle strain (10% ~ 60%), the applied stress induces the breakage and fragment of the lamellae, leading to the gradually reduced  $T_{m\beta}$  values. Furthermore, at high strain ( $> 60\%$ ), one should notice that the fusion of  $\alpha$ -iPP become broader with the increasing strain, which is different from the sharp fusion obtained in the normal conditions. This can be attributed to the broadening of the d-spacing distribution by deformation of crystals [38].

For other  $\beta$ -iPP with different content of  $\beta$ -phase nucleating agent, the similar melting behaviors of specimens as the function of strain are observed:  $\beta$ -phase predominates at low strain whereas  $\alpha$ -iPP predominates at high strain, suggesting the process of  $\beta/\alpha$  transformation during creep deformation. However, it is noticed that the intensity of the fusion peak of  $\beta$ -iPP is almost invariant at the beginning, suggesting that the content of  $\beta$ -iPP does not change at low strain ( $\leq 10\%$ ). This can be further shown by the variation of  $X_{c\beta}$  as shown in Figure 5. The  $X_{c\beta}$  shows the

similar variation trends in iPP/0.05TMB, iPP/0.2TMB, iPP/0.3TMB and iPP/0.6TMB. The content of  $\beta$ -phase tends to decrease monotonically to zero. However for  $\alpha$ -phase, the  $X_{c\alpha}$  tends to decrease firstly due to the breakup under stress and then increase with the increasing strain, finally achieve platform. This means that the different crystalline morphology of  $\beta$ -iPP have the similar crystalline structure evolution during creep deformation.

Figure 5 shows the variation of crystallinity with strain. For  $\beta$ -iPP, the  $X_{c\beta}$  decreases gradually whereas  $X_{c\alpha}$  increases with increasing strain, indicating the  $\beta/\alpha$  transformation. Furthermore, the  $X_c$  would slightly decrease at low strain and then increase slightly as the development of deformation. The slight decrease of  $X_c$  proves that the loss on the process of  $\beta$ - $\alpha$  transformation and the fragmentation of lamellar structure under stress. Obviously, the slightly increase of  $X_c$  in the following creep behavior is mainly attributed to the stress-induced crystallization.

Although the evolution of crystalline structure during deformation has been shown by DSC measurement, one should find that the  $\beta/\alpha$  transformation on the melting process should be an error to some extent in analyzing the DSC data. The  $\beta/\alpha$  transformation would result in higher value of  $\alpha$ -iPP crystallinity and relatively lower value of  $\beta$ -iPP crystallinity, especially at the beginning of the measurement. Therefore, to further prove the crystalline evolution got from DSC measurement, the variation of crystalline structure during creep were also investigated by XRD measurement, which are shown in Figure 6 and 7.

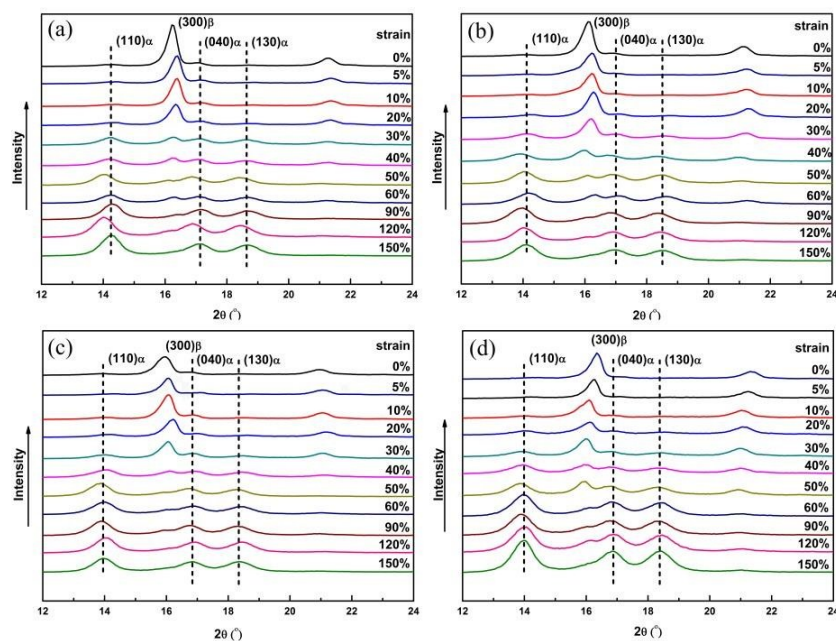


Figure 6 XRD patterns of (a) iPP/0.05TMB, (b) iPP/0.2TMB, (c) iPP/0.3TMB and (d) iPP/0.6TMB samples obtained at different strains as indicated on the graph.

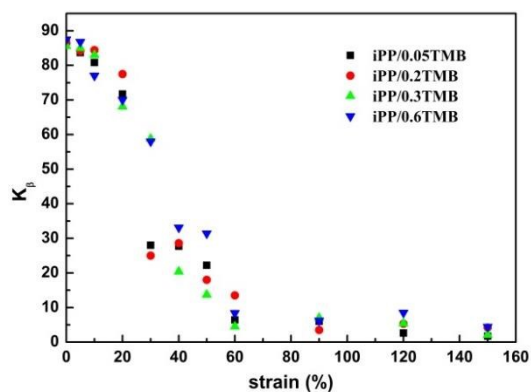


Figure 7 Variation of the relative crystallinity of  $\beta$ -phase as the function of strain.

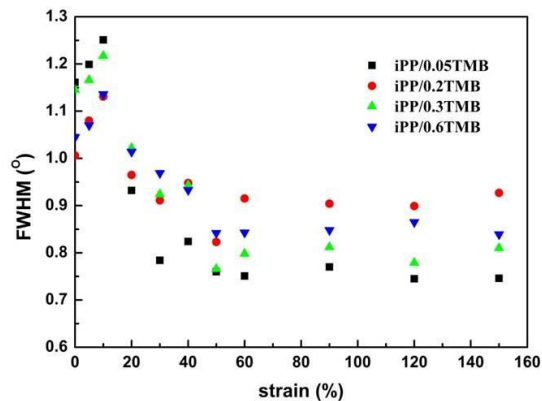


Figure 8 Variation of the full width at half maximum of 110-reflections as the function of strain.

From Figure 6 one can see that, the XRD profiles exhibit the typical characteristic diffraction at  $2\theta = 16.2^\circ$ ,  $21.2^\circ$ , indication of the (300) and (301) planes of  $\beta$ -iPP, respectively. Besides that, the characteristic diffraction peaks of the  $\alpha$ -iPP can be

differentiated at  $2\theta = 14.3$  (110), 17.1 (040), 18.7 (130). According to the results of XRD shown in Table 1, the relative contents of  $\beta$ -iPP in iPP/0.05TMB, iPP/0.2TMB, iPP/0.3TMB and iPP/0.6TMB samples are respectively calculated as 87.1%, 86.4%, 85.6% and 87.5%, indicating that different contents of  $\beta$ -phase nucleating agent have close content of  $\beta$ -phase. Furthermore, in Figure 7, all kinds of samples show the similar variation trend in the relative content of  $\beta$ -phase after being creep-deformed. In other words, the content of  $\beta$ -phase reduces gradually with the increasing strain, which is consistent with the result of DSC measurement. At first, when the strain is smaller than 10%, the intensity of  $K_{\beta\text{-XRD}}$  is little changed. This is same with the result showed in DSC measurement. One should notice that the platform of  $\beta$ -iPP diffractions at the start of creep (instantaneous deformation region) is mainly ascribed to the stretch between adjacent lamella leading to the orientation in the amorphous regions. Afterwards, there is a greatly reduced intensity of  $K_{\beta\text{-XRD}}$  when the strain increases higher than 10%. It shows the gradual increase of  $\alpha$ -iPP content and decrease of  $\beta$ -iPP content with strains, indicating the process of melting-recrystallization. After a sharp decline, the  $K_{\beta\text{-XRD}}$  of  $\beta$ -iPP reaches a platform at the strain around 60%. The intensity of  $\beta$ -iPP also nearly disappears in all kinds of samples, as shown in Figure 6.

Figure 8 shows the variation of the full width at half maximum (FWHM) of 110-reflections as the function of strain. At the small strain ( $\leq 10\%$ ), the crystallites are considered to become disordered remarkably as known from the increasing FWHM data. It would be ascribed to the deformation in the lamellar structure causing

by the stretch. At middle strain between 10% and 60%, the crystallites are considered to have better structural perfection with less disordered structure gradually due to the melting-recrystallization process. Finally, after the strain of 60%, the value of FWHM keeps invariant indicating the steady of crystalline structure. At this stage, the disentanglement of amorphous molecular chain undertakes the main deformation.

### Crystalline morphology change during deformation

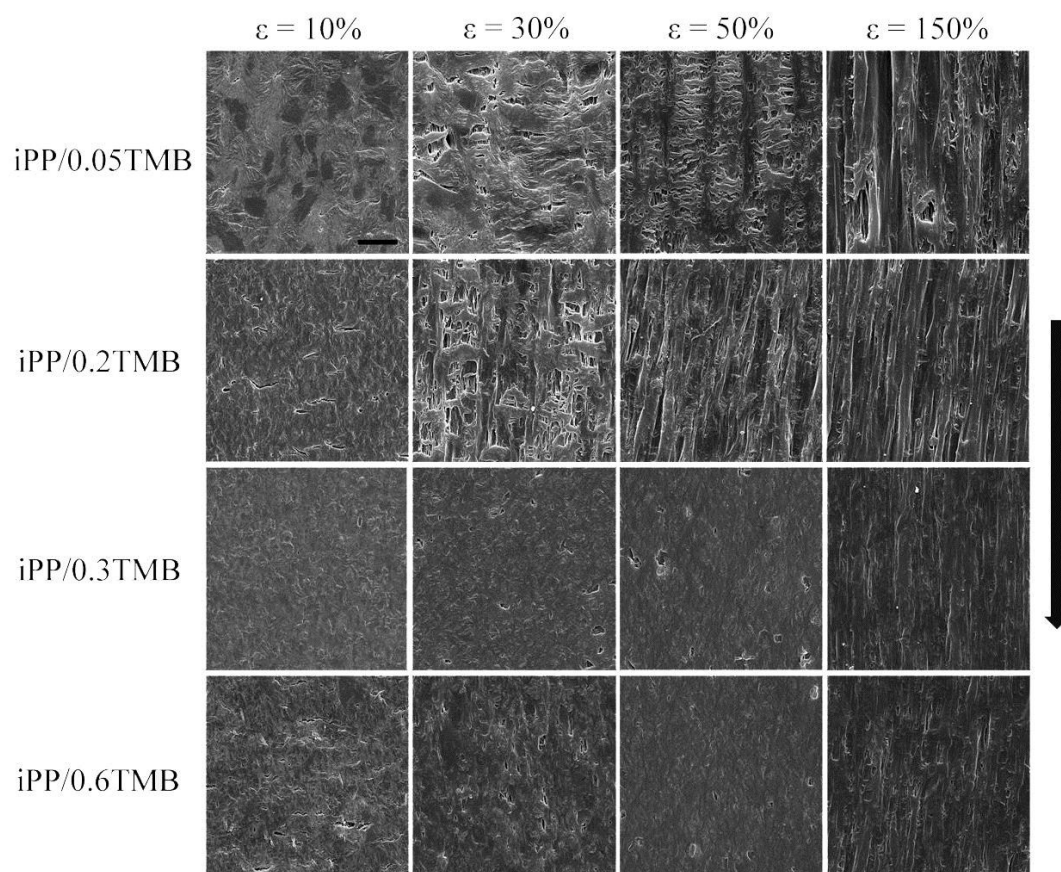


Figure 9 SEM photographs of the microstructures in iPP/0.05TMB, iPP/0.2TMB, iPP/0.3TMB and iPP/0.6TMB samples at different final strains:  $\epsilon = 10\%$ ,  $\epsilon = 30\%$ ,  $\epsilon = 50\%$  and  $\epsilon = 150\%$ . The tensile direction is vertical shown on the right. Scale bar denote  $10\mu\text{m}$ .

Figure 9 exhibits the microstructures of  $\beta$ -iPP obtained at different strains. Before creep, specimens with different contents of  $\beta$ -phase nucleating agent show the different supermolecular structures, which are consistent with the previous study, namely well-developed  $\beta$ -spherulites, bundle-like lamellar clusters and needle-like nucleating structure. At low strain of 10%, the samples begin to show clear crazes which explain the stress whitening during deformation. The typical crazes produced during creep have been showed in Figure 10. Crazes are cracks that remain bridged by fibrils of polymer and are perpendicular to the deformation direction [48-50], which has been shown in the Figure 9 and Figure 10. It is acknowledged that crazes are a sort of main localized plastic deformation mechanisms in semicrystalline polymers [51]. Recently, Castagnet et al. characterized PVDF by volumetric measurements during tensile test by SAXS [52]. They have shown that cavities would generate in the amorphous phase between lamella just before yielding. In our study, at low strain (10%), crazes exhibit on all kinds of samples, showing the direction perpendicular to the stress. Besides that, according to the results of DSC and XRD, the crystalline transformation only promotes in small degree under low strain (10%). Furthermore, the whole crystallization is little changed at this stage. Thus it is believed that the strain (10%) is too small to induce the process of melting-recrystallization. This is possibly due to the fact that in the instantaneous deformation region, specimens suffer the elastic stretch between adjacent lamella. Then in the primary creep and second creep regions, samples suffer the plastic deformation of crystallization. Namely, at small strains, the crystal mainly occur elastic and viscoelastic stretching to drive the

orientation of the interlamellar amorphous phase.

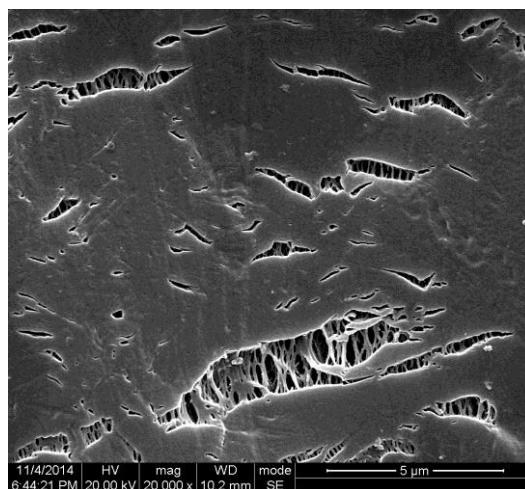


Figure 10 SEM photographs of the microstructures in iPP/0.05TMB at strain of 10%. The tensile direction is vertical.

At strain of 30%, the specimens suffer accelerating strain speed process. The crystalline transformation and the tensile deformation make the crystalline morphology irregular. The crystalline morphologies become disorder in all kinds of  $\beta$ -iPP. For iPP/0.05TMB sample, the well-developed  $\beta$ -spherulites change and tend to break into fragments. Furthermore, some large slits can be seen which cross the whole spherulites and the boundaries. For iPP/0.2TMB specimen, the bundle-like morphology becomes inconspicuous. And some large slits are further stretched along the stress direction, leading to the direction of the crazes transform to the tensile direction gradually. Besides, initial fiber-like structure occurs in this stage. Namely, the strain of 30% induces greatly change of the crystalline morphology in iPP/0.2TMB specimen. Compared to the obvious tensile deformation of crazes and crystallization in iPP/0.05TMB and iPP/0.2TMB, the microstructures have little change in iPP/0.3TMB and iPP/0.6TMB specimens. It can be deduced to that the higher contents of  $\beta$ -phase nucleating agent would prevent the further growth of

crazes. On the other hand, iPP/0.2TMB and iPP/0.3TMB have the similar level of creep resistance, which means that the growth of crazes do not affect the creep resistance of samples.

At strain of 50%, both iPP/0.05TMB and iPP/0.2TMB exhibit more serious defects. For iPP/0.05TMB specimen, the well-developed  $\beta$ -spherulites are no longer observed. Contrarily, a large number of slits can be seen due to the fragmentation and separation of crystallization structure. The slits start to orient at this strain. It was observed that cavities firstly grow perpendicular to the applied stress and then elongate in the direction of the stress [53]. For iPP/0.2TMB specimen, the size of oriented slits is much smaller than that observed at the strain of 30%. This is possibly due to the decrease of cross section, leading to the shrink of apertures in the fiber-like structure. As to iPP/0.3TMB and iPP/0.6TMB specimens, there are larger crazes and slightly oriented fragmentation showed in the SEM pictures. However, the orientation in these specimens is still unclear.

With further increasing of the strain (150%), all iPP/0.05TMB, iPP/0.2TMB, iPP/0.3TMB and iPP/0.6TMB samples exhibit highly oriented structure. The fiber-like structure is deduced to oriented crystal, namely newly formed  $\alpha$ -phase, which has relatively smooth surface feature. Obviously, the entanglement of molecular chain most likely contributes to accelerating fracture observed at the last stage of creep deformation after creep fatigue failure point.

### **PALS results**

The fourth component got from the results of PALS, attributed to pick-off annihilation of o-Ps formed in the free-volume local holes, depends on the dimension of the free volume local hole where the positron is localized forming Ps state [54,55]. The fourth lifetime,  $\tau_4$ , and the relative intensity,  $I_4$ , are given in Figure 11.  $\tau_4$  positively relates to the electron density of free volume and negatively associates with the free volume radius (R).  $\tau_4$  could be calculated by a semiempirical equation:

$$\tau_4 = \frac{1}{2} \left[ 1 - \frac{R}{R + \Delta R} + \frac{1}{2\pi} \sin \left( \frac{2\pi R}{R + \Delta R} \right) \right]^{-1} \quad (4)$$

Where  $\tau_4$  is given in nanoseconds and  $\Delta R$  is the thickness of a homogeneous electron layer surrounding the free volume hole where the Ps annihilates, so that  $R + \Delta R$  is the radius of the spherical potential wells corresponding to the free volume hole.  $\Delta R = 0.166$  nm is usually assumed for polymers according to experimental results in zeolites and molecular solids [56]. Through equation (4), the free volume radius is obtained, as shown in Figure 11 as well.

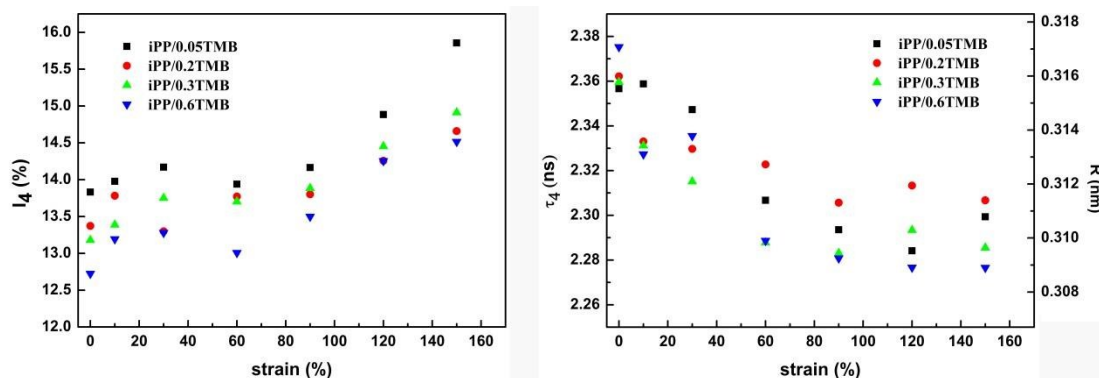


Figure 11 Lifetime ( $\tau_4$ ) and intensity ( $I_4$ ) of the fourth component as the function of strain for  $\beta$ -iPP during creep.

For all types of  $\beta$ -iPP having different contents of nucleating agent, the fourth component has the similar variation. At small strain ( $\leq 10\%$ ),  $\tau_4$  decreases and  $I_4$

reflecting the Ps formation probability in the free volume holes increases. This is might be due to the breakup of the free volume during deformation showing as the increase in size while decrease in number for the free volume. At middle strain (10%~60%),  $\tau_4$  goes down fast but  $I_4$  increases slightly exhibiting a similar variation trend of free volume in pure iPP [39]. Because of polymer chains with larger free volume owning stronger mobility, it would be easier to orient and rearrange for the chains when the melt-recrystallization process occurs, which generates the decrease of  $\tau_4$ . At high strain ( $\geq 60\%$ ),  $\tau_4$  slightly reduces and  $I_4$  greatly increases. It would be attributed to that the further deformation of the chains with more defects generated in amorphous region results in the increasing of the number of free volume holes. The variety of  $\tau_4$  and  $I_4$  on different stages reflects the change of free volume, which would provide a view for the evolution of amorphous region during creep deformation.

## Conclusions

In summary, the crystalline transformation has been observed by DSC and XRD measurements during the creep deformation. Besides, the change of crazes and the generating of the fiber-like structure during deformation are observed by SEM measurement. It is interesting to find out that the higher content of  $\beta$ -phase nucleating agent would hinder the growth of crazes. Furthermore, the changes of free volume during deformation have been explored by PALS, showing the microscopic changing of amorphous region. For iPP/0.05TMB specimen, the well-developed  $\beta$ -spherulites

achieved by critical content of  $\beta$ -phase nucleating agent show lowest creep resistance compared with other specimens. For iPP/0.2TMB and iPP/0.3TMB samples with bundle-like morphology, they have higher creep-resistant ability than iPP/0.05TMB specimen and lower than iPP/0.6TMB specimen with needle-like nucleation structure achieved by supercritical content of  $\beta$ -phase nucleating agent. During creep behavior, the lamella of all  $\beta$ -iPP exhibit elastic/plastic deformation at the beginning of creep (strain  $\leq 10\%$ ), just before the point of fatigue failure, which can be deduced to the movement in amorphous regions. Subsequently, at the strain between 11% and 60%, a crystalline transformation phenomenon appears after the point of creep fatigue failure (strain = 11%). As the results of DSC and XRD show that, the samples with different contents of  $\beta$ -phase nucleating agent have the same variation trend in crystalline transformation. Besides that, SEM measurement shows that more content of  $\beta$ -phase nucleating agent would restrain the growth of the caves, but have no direct effect on the creep resistance. This is believed that the crystal morphology with different long spacing is the main factor in determining the creep resistance. Finally, after the strain of 60%, stretched-induced oriented crystal shows up.

## Acknowledgments

This project is supported by the National Natural Science Foundation of China (No. 51133005 and 51421061), and the Research Fund for the Doctoral Program of Higher Education (No. 20120181130013).

## References

1. Grein C, Plummer C J G, Kausch H H, et al. Influence of  $\beta$  nucleation on the mechanical properties of isotactic polypropylene and rubber modified isotactic polypropylene[J]. *Polymer*, 2002, 43(11): 3279-3293.
2. Grein C. Toughness of neat, rubber modified and filled  $\beta$ -nucleated polypropylene: from fundamentals to applications[M]//*Intrinsic Molecular Mobility and Toughness of Polymers II*. Springer Berlin Heidelberg, 2005: 43-104.
3. Varga J.  $\beta$ -Modification of isotactic polypropylene: preparation, structure, processing, properties, and application[J]. *Journal of Macromolecular Science, Part B*, 2002, 41(4-6): 1121-1171.
4. Varga J. Supermolecular structure of isotactic polypropylene[J]. *Journal of Materials Science*, 1992, 27(10): 2557-2579.
5. Lotz B, Wittmann J C, Lovinger A J. Structure and morphology of poly(propylenes): a molecular analysis[J]. *Polymer*, 1996, 37(22): 4979-4992.
6. Lotz B, Graff S, Straupe C, et al. Single crystals of  $\gamma$  phase isotactic polypropylene: combined diffraction and morphological support for a structure with non-parallel chains[J]. *Polymer*, 1991, 32(16): 2902-2910.
7. Varga J, Karger-Kocsis J. The occurrence of transcrystallization or row-nucleated cylindritic crystallization as a result of shearing in a glass-fiber-reinforced polypropylene[J]. *Composites science and technology*, 1993, 48(1): 191-198.
8. Varga J, Karger-Kocsis J. Rules of supermolecular structure formation in sheared isotactic polypropylene melts[J]. *Journal of Polymer Science-B-Polymer Physics Edition*, 1996, 34(4): 657-670.
9. LEUGERIN. HJ, Kirsch G. Effect of crystallization from oriented melts on crystal-structure of isotactic polypropylene[J]. *Angewandte Makromolekulare Chemie*, 1973, 33(OCT): 17-23.
10. Somani R H, Hsiao B S, Nogales A, et al. Structure development during shear flow induced crystallization of i-PP: in situ wide-angle X-ray diffraction study[J]. *Macromolecules*, 2001, 34(17): 5902-5909.
11. Huo H, Jiang S, An L, et al. Influence of shear on crystallization behavior of the  $\beta$  phase in isotactic polypropylene with  $\beta$ -nucleating agent[J]. *Macromolecules*, 2004, 37(7): 2478-2483.
12. Crissman J M. Mechanical relaxation in polypropylene as a function of polymorphism and degree of lamella orientation[J]. *Journal of Polymer Science Part A - 2: Polymer Physics*, 1969, 7(2): 389-404.
13. Fujiwara Y. Das doppelschmelzverhalten der $\beta$ -Phase des isotaktischen polypropylens[J]. *Colloid and Polymer Science*, 1975, 253(4): 273-282.
14. Varga J.  $\beta$ -Modification of isotactic polypropylene: preparation, structure, processing, properties, and application[J]. *Journal of Macromolecular Science, Part B*, 2002, 41(4-6): 1121-1171.
15. Varga J, Menyhard A. Effect of solubility and nucleating duality of N, N'-dicyclohexyl-2, 6-naphthalenedicarboxamide on the supermolecular structure of isotactic polypropylene[J]. *Macromolecules*, 2007, 40(7): 2422-2431.
16. Varley R J, Dell'Olio M, Yuan Q, et al. Different  $\beta$  nucleants and the resultant microstructural, fracture, and tensile properties for filled and unfilled ISO

- polypropylene[J]. *Journal of Applied Polymer Science*, 2013, 128(1): 619-627.
17. Tjong S C, Shen J S, Li R K Y. Mechanical behavior of injection molded  $\beta$  - crystalline phase polypropylene[J]. *Polymer Engineering & Science*, 1996, 36(1): 100-105.
  18. Tordjeman P, Robert C, Marin G, et al. The effect of  $\alpha$ ,  $\beta$  crystalline structure on the mechanical properties of polypropylene[J]. *The European Physical Journal E*, 2001, 4(4): 459-465.
  19. Grein C. Toughness of neat, rubber modified and filled  $\beta$ -nucleated polypropylene: from fundamentals to applications[M]//*Intrinsic Molecular Mobility and Toughness of Polymers II*. Springer Berlin Heidelberg, 2005: 43-104.
  20. Wu T, Xiang M, Cao Y, et al. Influence of lamellar structure on the stress–strain behavior of  $\beta$  nucleated polypropylene under tensile loading at elevated temperatures[J]. *RSC Advances*, 2015, 5(54): 43496-43507.
  21. Münstedt H. Rheological experiments at constant stress as efficient method to characterize polymeric materials[J]. *Journal of Rheology (1978-present)*, 2014, 58(3): 565-587.
  22. Lin C, Liu J, Gong F, et al. High-temperature creep properties of TATB-based polymer bonded explosives filled with multi-walled carbon nanotubes[J]. *RSC Advances*, 2015, 5(27): 21376-21383.
  23. Osman A F, Andriani Y, Edwards G A, et al. Engineered nanofillers: impact on the morphology and properties of biomedical thermoplastic polyurethane nanocomposites[J]. *RSC Advances*, 2012, 2(24): 9151-9164.
  24. Alavijeh A S, Khorasany R M H, Habisch A, et al. Creep properties of catalyst coated membranes for polymer electrolyte fuel cells[J]. *Journal of Power Sources*, 2015, 285: 16-28.
  25. ASTM D 2990-01. Standard test methods for tensile, compressive, and flexural creep and creep-rupture of plastics. West Conshohocken: ASTM International; 2001.
  26. Drozdov A D, Lejre A L H. Viscoelasticity, viscoplasticity, and creep failure of polypropylene/clay nanocomposites[J]. *Composites Science and Technology*, 2009, 69(15): 2596-2603.
  27. Drozdov A D. Creep failure of polypropylene: experiments and constitutive modeling[J]. *International journal of fracture*, 2009, 159(1): 63-79.
  28. Drozdov A D. Creep rupture and viscoelastoplasticity of polypropylene[J]. *Engineering Fracture Mechanics*, 2010, 77(12): 2277-2293.
  29. Lee H N, Riggleman R A, de Pablo J J, et al. Deformation-induced mobility in polymer glasses during multistep creep experiments and simulations[J]. *Macromolecules*, 2009, 42(12): 4328-4336.
  30. Vas L M, Bakonyi P. Estimating the creep strain to failure of PP at different load levels based on short term tests and Weibull characterization[J]. *Express Polymer Letters*, 2012, 6(12): 987-996.
  31. Peterlin A. Molecular model of drawing polyethylene and polypropylene[J]. *Journal of materials science*, 1971, 6(6): 490-508.
  32. Peterlin A. Plastic deformation of polymers with fibrous structure[J]. *colloid and Polymer Science*, 1975, 253(10): 809-823.

33. Jiang Z, Tang Y, Men Y, et al. Structural evolution of tensile-deformed high-density polyethylene during annealing: scanning synchrotron small-angle X-ray scattering study[J]. *Macromolecules*, 2007, 40(20): 7263-7269.
34. Jiang Z, Tang Y, Rieger J, et al. Two lamellar to fibrillar transitions in the tensile deformation of high-density polyethylene[J]. *Macromolecules*, 2010, 43(10): 4727-4732.
35. Monge M A, Diaz J A, Pareja R. Strain-induced changes of free volume measured by positron lifetime spectroscopy in ultrahigh molecular weight polyethylene[J]. *Macromolecules*, 2004, 37(19): 7223-7230.
36. Cheng K M, Tian C, Du Y, et al. Effect of OPS Dispersion Method on the Free Volume of Polyurethane by Positron Annihilation Lifetime Spectroscopy (PALS)[J]. *Polymer-Plastics Technology and Engineering*, 2012, 51(4): 396-400.
37. Brown E N, Dattelbaum D M, Brown D W, et al. A new strain path to inducing phase transitions in semi-crystalline polymers[J]. *Polymer*, 2007, 48(9): 2531-2536.
38. Brown E N, Clausen B, Brown D W. In situ measurement of crystalline lattice strains in phase IV polytetrafluoroethylene[J]. *Journal of Neutron Research*, 2007, 15(2): 139-146.
39. Jia C, Zhang Q, Liao X, et al. Hierarchical microstructure changes and the molecular mechanism of polypropylene under a critical failure strain during creep[J]. *Polymer*, 2015, 67: 92-100.
40. Strobl G R, Schneider M. Direct evaluation of the electron density correlation function of partially crystalline polymers[J]. *Journal of Polymer Science: Polymer Physics Edition*, 1980, 18(6): 1343-1359.
41. Li J X, Cheung W L, Jia D. A study on the heat of fusion of  $\beta$ -polypropylene[J]. *Polymer*, 1999, 40(5): 1219-1222.
42. Liu M, Guo B, Du M, et al. Halloysite nanotubes as a novel  $\beta$ -nucleating agent for isotactic polypropylene[J]. *Polymer*, 2009, 50(13): 3022-3030.
43. Turner Jones A, Aizlewood JM, Beckett DR (1964) Crystalline forms of isotactic polypropylene. *Makromol Chem* 75:134–158
44. Dong M, Guo Z, Su Z, et al. Study of the crystallization behaviors of isotactic polypropylene with sodium benzoate as a specific versatile nucleating agent[J]. *Journal of Polymer Science Part B: Polymer Physics*, 2008, 46(12): 1183-1192.
45. Dong M, Guo Z, Yu J, et al. Crystallization behavior and morphological development of isotactic polypropylene with an aryl amide derivative as  $\beta$  - form nucleating agent[J]. *Journal of Polymer Science Part B: Polymer Physics*, 2008, 46(16): 1725-1733.
46. Dong M, Guo Z X, Yu J, et al. Study of the assembled morphology of aryl amide derivative and its influence on the nonisothermal crystallizations of isotactic polypropylene[J]. *Journal of Polymer Science Part B: Polymer Physics*, 2009, 47(3): 314-325.
47. Menyárd A, Varga J. The effect of compatibilizers on the crystallisation, melting and polymorphic composition of  $\beta$ -nucleated isotactic polypropylene and polyamide 6 blends[J]. *European polymer journal*, 2006, 42(12): 3257-3268.
48. Friedrich, K. Crazes and shear bands in semi-crystalline thermoplastics. *Adv.*

Polym. Sci. 1983, 225–274.

49. Kausch H H, Gensler R, Grein C, et al. Crazing in semicrystalline thermoplastics[J]. *Journal of Macromolecular Science—Physics*, 1999, 38(5-6): 803-815.

50. Narisawa I, Ishikawa M. Crazing in semicrystalline thermoplastics[M]//*Crazing in Polymers Vol. 2*. Springer Berlin Heidelberg, 1990: 353-391.

51. Bowden P B, Young R J. Deformation mechanisms in crystalline polymers[J]. *Journal of Materials Science*, 1974, 9(12): 2034-2051.

52. Castagnet S, Girault S, Gacougnolle J L, et al. Cavitation in strained polyvinylidene fluoride: mechanical and X-ray experimental studies[J]. *Polymer*, 2000, 41(20): 7523-7530.

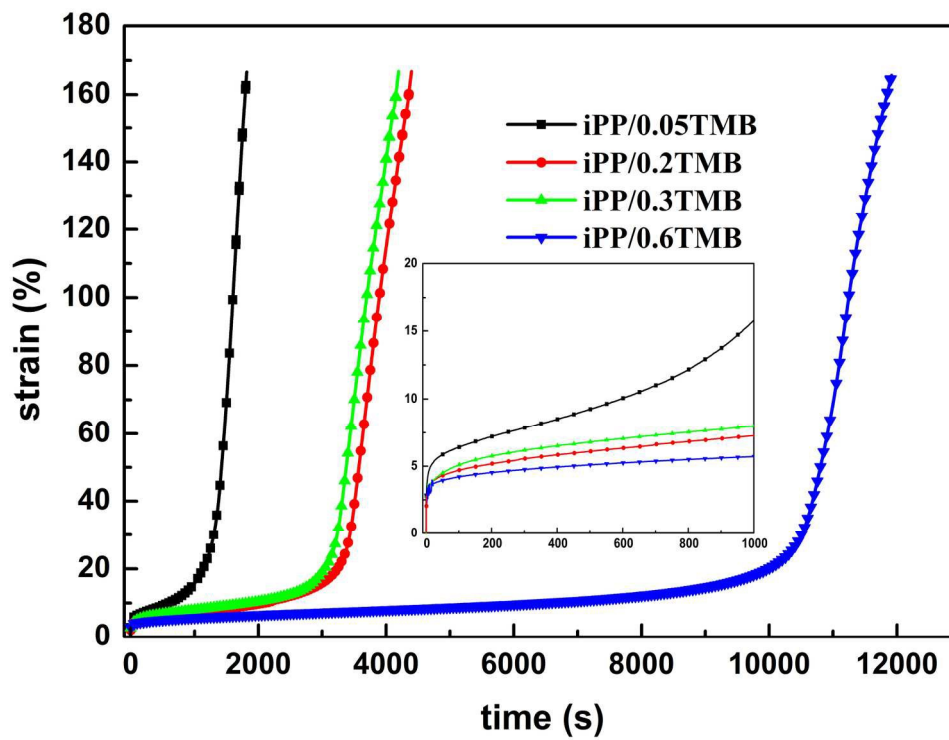
53. Lairinandrasana L, Morgeneyer T F, Proudhon H, et al. Effect of multiaxial stress state on morphology and spatial distribution of voids in deformed semicrystalline polymer assessed by x-ray tomography[J]. *Macromolecules*, 2012, 45(11): 4658-4668.

54. Kirkegaard P, Pedersen N J, Eldrup M M. PATFIT-88: a data-processing system for positron annihilation spectra on mainframe and personal computers[M]. 1989.

55. Mogensen O E. Positron annihilation in chemistry[M]. Berlin: Springer-Verlag, 1995.

56. Nakanishi H, Wang S J, Jean Y C, et al. Positron annihilation studies of fluids[J]. World Science, Singapore, 1988, 292.

This manuscript investigates the creep performance of  $\beta$ -iPP with different crystalline morphologies.



174x128mm (300 x 300 DPI)